

Validation and verification of RANS solvers for TUDa-GLR-OpenStage transonic axial compressor

Original article

Article history:

Submission date: 18 July 2022

Final revision date: 11 November 2022

Acceptance date: 21 December 2022

Publication date: 27 January 2023

This is the updated version of a paper originally presented at the Global Power and Propulsion Virtual Technical Conference, GPPS Xi'an21, April 11–13, 2022



*Correspondence:

XH: xiao.he2014@imperial.ac.uk

Peer review:

Single blind

Copyright:

© 2023 He et al. © This is an open access article distributed under the Creative Commons Attribution License (CC-BY 4.0), which permits unrestricted use, distribution, and reproduction in any medium, provided the original work is properly cited and its authors credited.

Keywords:

Transonic compressor; CFD; Validation and Verification; RANS Turbulence Modeling

Citation:

He X., Zhu M., Xia K., Fabian K. S., Teng J., and Vahdati M. (2023). Validation and verification of RANS solvers for TUDa-GLR-OpenStage transonic axial compressor. *Journal of the Global Power and Propulsion Society*. 7: 13–29.
<https://doi.org/10.33737/jgpps/158034>

Xiao He^{1,†,*}, Mingmin Zhu^{2,†}, Kailong Xia², Klausmann Sebastian Fabian³, Jinfang Teng², Mehdi Vahdati¹

¹Department of Mechanical Engineering, Imperial College London, London SW7 2AZ, UK

²School of Aeronautics and Astronautics, Shanghai Jiao Tong University, Shanghai 200240, China

³Institute of Gas Turbines and Aerospace Propulsion, Technische Universität Darmstadt, Darmstadt 64287, Germany

[†]The authors contributed equally to this work.

Abstract

This paper presents a comprehensive validation and verification study of turbomachinery Reynolds-averaged Navier-Stokes flow solvers on the transonic axial compressor TUDa-GLR-OpenStage. Two commercial solvers namely Ansys CFX and Numeca FineTurbo are adopted to provide the benchmark solutions, which can be used for verification of other RANS solvers in the future. Based on these solvers, five sets of grids, two advection schemes (i.e., central difference and second-order upwind), four turbulence models (i.e., SA, SA-RC, SST and EARSM) and two rotor-stator interface models (i.e., mixing plane and sliding plane) are investigated to quantify their effects on predicting the performance and the flow field of the compressor stage. Results show that the choices of grid density and turbulence model are most sensitive to the prediction, leading to 5% and 7% variation in compressor performance characteristics, respectively. Regarding the choice of grid density, a method to estimate the grid discretization error is demonstrated, which is transferrable to other cases. Regarding the choice of turbulence model, the EARSM model is found overall most accurate among the investigated models, and the limitations and deficiencies of the rest models are discussed in detail based on the analysis of the mean flow fields and the eddy viscosity fields. The grids and the major CFD results presented in this work are open-accessed to the community for further research. The results and discussions presented in this paper provide a useful reference for future practices of RANS simulations for compressors.

Introduction

Reynolds-averaged Navier-Stokes (RANS) simulation is the industrial workhorse for predicting turbomachinery flows, but users can occasionally find inconsistencies in RANS solvers such as:

- Using the “same” numerical settings from different RANS solvers can predict different results.
- Each RANS solver has a “best-practice” list of numerical settings based on previous user experience, but this list may vary from one solver to another.
- When using the “best-practice” settings of a solver, the quantity of interest may be over-predicted in one case and under-predicted in another, despite the flow phenomena of the cases being similar.

These inconsistencies not only undermine users' trust in the RANS solvers but also hinder developers from understanding and improving the numerical models used in RANS simulations.

The source of RANS solver inconsistencies can be rooted back to the uncertainties and errors in experiments and simulations. In terms of experiments, uncertainties and errors in geometries and test instruments vary for different test cases and test rigs; in some cases, the experimental uncertainties and errors may be pronounced enough to overwhelm the difference in RANS results. In terms of simulations, the prediction is subjected to many user-specified numerical settings; comparisons among different RANS solvers at the same numerical settings are seldom reported due to user preference (i.e., following the "best-practice" guideline of a specific solver), coding preference (e.g., an in-house variant of a model is implemented instead of the original one) and potential coding errors.

To tackle the issue of RANS solver inconsistency, a series of validation and verifications (V&V) studies of RANS solvers are crucial. Following the definitions from the American Institute of Aeronautics and Astronautics (AIAA) ([Computational Fluid Dynamics Committee, 1998](#)):

- Validation is the process of determining the degree to which a model is an accurate representation of the real world from the perspective of the intended uses of the model.
- Verification is the process of determining that a model implementation accurately represents the developer's conceptual description of the model and the solution to the model.

In other words, validation compares simulation results against measured data, which quantifies the simulation accuracy; verification can be performed by comparing simulation results from different codes with each other, which helps exclude potential coding errors. Verification is the first step toward a successful validation study.

V&V studies have drawn attention from the general aerospace sector for the past ten years ([Rumsey et al., 2010](#)). In response, the NASA Turbulence Modeling Resource (TMR) website ([Rumsey, 2021](#)) was established, which serves as an open repository of RANS turbulence model documentation and V&V test cases. However, V&V studies have not yet received as much attention in the turbomachinery community as in the external flow community. The last major V&V campaign for compressor flows dates back to the 1994 International Gas Turbine Institute (IGTI) blind test on the NASA Rotor 37 ([Denton, 1997](#)), along with many individual validation efforts on other NASA compressor geometries ([Suder, 2021](#)) over the years. From today's perspective, the measurement accuracy of these data may no longer present state-of-the-art. Online and version-controlled documentation of these geometries and measured data was also not achieved due to the limitations of the times—users today need to find the most updated geometries and data from pieces of literature by themselves (e.g., characteristics and tip gap size of NASA Rotor 67 ([Grosvenor, 2007](#))), and some details of the geometry are still not known (e.g., running tip gap size of rotors, hub cavity geometry of stators). In addition, it is challenging to conclude from the early V&V campaign due to a lack of solver verification ([Denton, 1997](#)). Therefore, a new V&V campaign of turbomachinery RANS solvers based on recent common research models of compressors is of high interest.

In the 2020 GPPS Chania conference, the Institute of Gas Turbines and Aerospace Propulsion (GLR) of Technische Universität Darmstadt released the TUDa-GLR-OpenStage transonic axial compressor including the geometry in digitized form and an abundant set of measurement data ([Klausmann et al., 2021](#)). This is an ideal compressor test case for RANS V&V purposes. In this work, established commercial turbomachinery RANS solvers are performed on this case to provide the benchmark solutions. These benchmark solutions along with the associated grids and boundary conditions will be released to the public for future verification of other RANS solvers. Based on the commercial solvers, the effects of grid density, advection scheme, turbulence model and rotor-stator interface model on predicting the TUDa-GLR-OpenStage case are investigated. These results will be presented after introducing the experimental and numerical setup of the case.

Methodology

Case description

The investigated TUDa-GLR-OpenStage is a single-stage high-speed axial compressor, which represents a typical front stage of a high-pressure compressor in a commercial turbofan engine. The compressor stage consists of a blisk rotor with radially stacked CDA-airfoils, a stator with optimized 3D shapes, and an outlet guide vane (OGV) that straightens the flow. The rotor is originally designed by MTU and first tested in 1994. It has been investigated extensively in a series of previous experimental and numerical works ([Hoeger et al., 1999](#); [Bergner et al., 2006](#); [Muller et al., 2011](#)). The rotor blades are highly cambered near the hub and thin near the tip. The

running tip gap size is approximately 0.75 mm at the design condition, and the hub fillet radius is 5 mm. The stator is designed conjointly between the GLR and the German Aerospace Center (DLR). It is optimized via an automated multi-objective optimization process to suppress the separation size (Bakhtiari et al., 2015). The stator blades have a forward sweep feature near both endwalls and a bow feature towards the pressure surface near the casing. The shapes of the fillets at both endwalls are prescribed by a digitized geometry file. More details about the investigated stage are summarized in Table 1.

Test rig

The TUDa-GLR-OpenStage was tested on the transonic compressor rig of GLR, which can measure the steady-state performance, the aerodynamic instabilities and the blade vibration levels of the compressors. The schematic of the test facility is shown in Figure 1. The inlet flow passes through an inlet throttle, a settling chamber and a mass flow measurement section before reaching the compressor core. The compressor is driven by a DC motor with a gearbox. Shaft input torque and rotor speed is measured using a torque meter.

The measurement sections of the compressor are also marked in Figure 1. At the stage inlet section (ME15), radial profiles of total pressure and total temperature are measured. At the rotor exit section (ME21), radial profiles of total pressure and absolute Mach number components are available. At the stage exit section (ME30), 2D distributions of total pressure and total temperature are acquired. The total pressure ratio and total temperature ratio characteristics are calculated by the area-averaged probe data at sections ME15 and ME30; the isentropic efficiency is calculated using the probe-based total pressure ratio and the shaft power. For a fair comparison between the experiment and CFD, the isentropic efficiency from CFD is calculated based on the area-averaged pressure ratio and the mass-averaged temperature ratio. Calculations of the measurement uncertainty along with the measured data are detailed in the concurrent experimental work (Klausmann et al., 2021).

The measurements were performed at 100%, 80% and 65% design speed. This work mainly focuses on the 100% design speed at the peak-efficiency (PE) condition ($m = 16.00 \pm 0.02$ kg/s) and the near-stall (NS) condition ($m = 14.78 \pm 0.02$ kg/s).

Table 1. Design parameters of TUDa-GLR-OpenStage (Klausmann et al., 2021).

Parameters	Symbols	Values
Rotor tip Mach number	M_t	1.17
Rotor mean aspect ratio	$(r_t - r_h)/c_m$	0.94
Rotor hub-to-tip ratio	r_h/r_t	0.51
Rotor tip gap-to-chord ratio	τ/C_t	0.8%
Rotor tip radius (mm)	r_t	190
Rotor tip chord length (mm)	c_t	94
Rotor design speed (RPM)	N	20000
Stage flow coefficient	ϕ	0.37
Stage loading coefficient	ψ	0.40
Stage mass flow (kg/s)	m	16.0
Stage total pressure ratio	π	1.50
Number of blades	Z	16/29/5

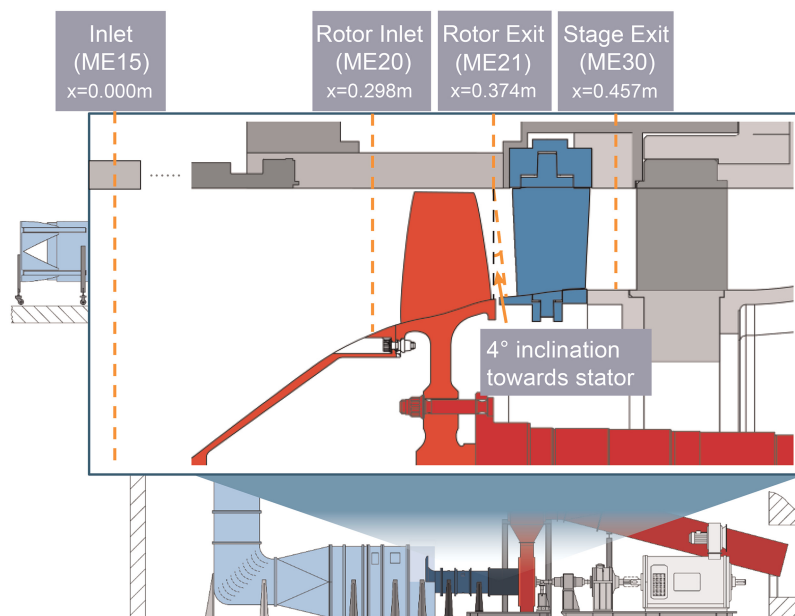


Figure 1. Illustration of TUDa-GLR-OpenStage test rig.

CFD solvers

In this work, two widely used commercial RANS flow solvers are adopted: Ansys CFX 20.1 and Numeca FineTurbo 14.1.

Ansys CFX uses an element-based finite volume method to discretize the RANS equations based on unstructured meshes. The diffusion term is discretized by the second-order accurate central scheme, and the advection term is discretized by the second-order accurate high resolution scheme. The temporal discretization is achieved by the second-order accurate backward Euler scheme. The linearized equations are solved by the Incomplete Lower Upper (ILU) factorization technique, which is accelerated by an algebraic multigrid method. A pseudo time-stepping algorithm with an automatic time scale technique is used for steady-state calculations. For best-practice of turbomachinery simulation, the updated Menter $k - \omega$ shear stress transport (SST) turbulence model (Menter et al., 2003) (i.e., “SST-2003” (Rumsey, 2021)) is recommended. The Spalart-Allmaras (SA) turbulence model (Spalart and Allmaras, 1994) (i.e., “SA-noft2” (Rumsey, 2021)) is also available. More details about the solver can be found in its user guide (ANSYS, 2021).

Numeca FineTurbo discretizes the RANS equations using a cell-centered control volume approach based on structured meshes. The diffusion term is discretized by the second-order accurate central scheme. The advection term is discretized by either the central scheme with a Jameson-Schmidt-Turkel (JST) type dissipation term (Jameson et al., 1981) or the upwind scheme using flux difference splitting from Roe (1981), both of which are second-order accurate. The temporal discretization is achieved by the explicit fourth-order accurate Runge-Kutta integration scheme. For steady-state cases, the pseudo time-stepping algorithm is used. Local time stepping, implicit residual smoothing, and multigrid techniques are applied to accelerate convergence. The modified SA turbulence model (Ashford, 1996) (i.e., “SA-fv3-noft2”¹ (Rumsey, 2021)) is set as the default for turbomachinery simulations. Other turbulence models including the modified SARC model (Shur et al., 2000) (i.e., “SA-RC-fv3-noft2” (Rumsey, 2021)), the original SST model (Menter, 1994) (i.e., “SST” (Rumsey, 2021)) and the simplified baseline EARSM model (Menter et al., 2012) are also available. More details of the solver can be found in its user guide (NUMECA International, 2021).

Flow domain, boundary conditions and grids

The simulation is conducted by using a single-passage flow domain with the circumferentially periodic boundary condition, as illustrated in Figure 2a. The inlet plane is set at the stage inlet section ME15. The measured total pressure and total temperature profiles are used to prescribe the inlet boundary condition. In addition, the inlet flow direction is axial; the turbulence intensity and turbulence length scale are estimated as 4% and 0.09 mm

¹ The “fv3” modification was an early attempt to avoid negative ν_t , but should now be deprecated due to its unusual transition behavior at low Re (Rumsey et al., 2010).

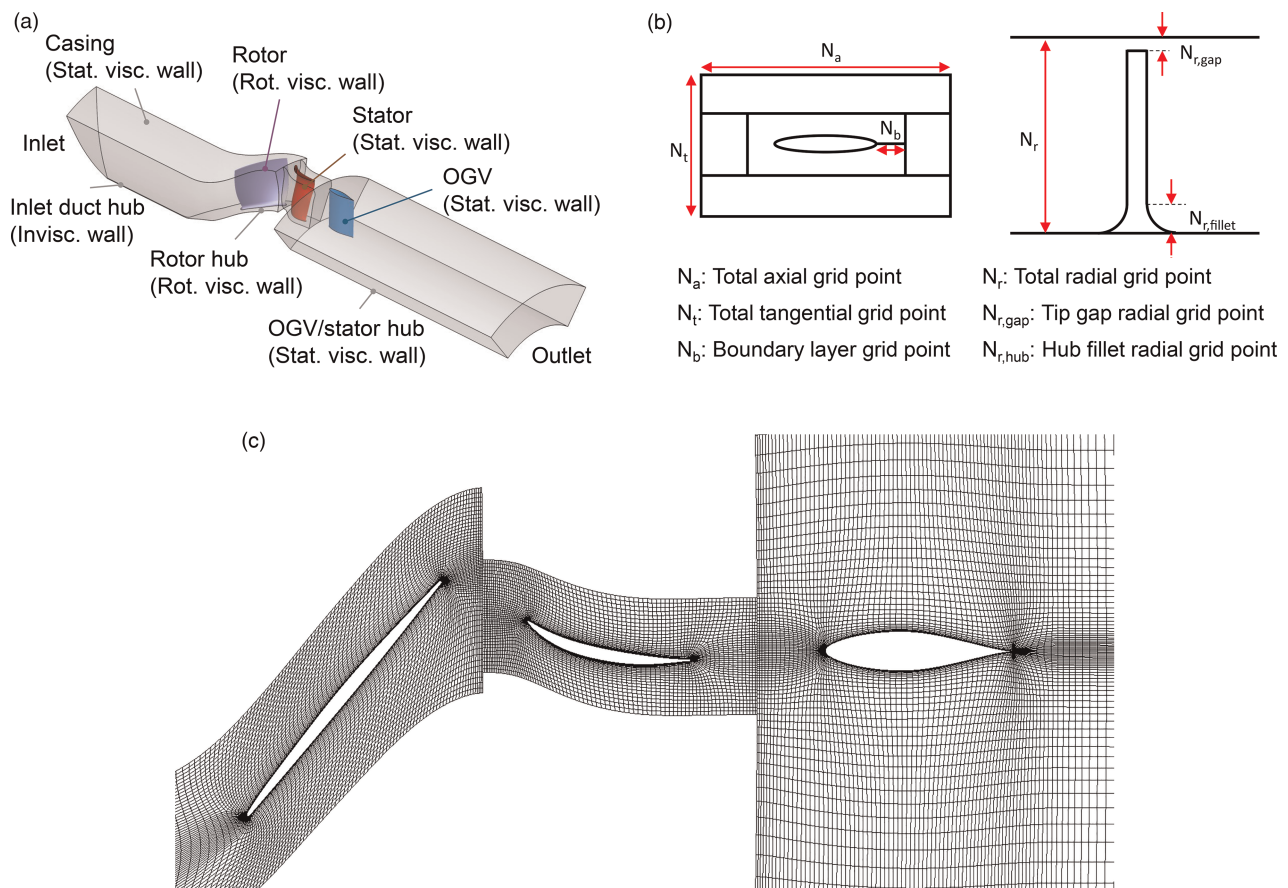


Figure 2. Illustration of TUDa-GLR-OpenStage CFD model. (a) Flow domain and boundary conditions (b) Grid topology (c) Visualization of the Medium grid at mid-span.

respectively, which are equivalent to an eddy viscosity ratio of 35. At the rotor-stator and the stator-OGV interface, a mixing plane boundary condition (specifically, “Stage (Mixing-Plane)” with “Constant Total Pressure” as downstream velocity constraint for Ansys CFX; “Full Non-Matching Mixing Plane” for Numeca FineTurbo) is used. The outlet boundary is set at the location about 1.5 times the compressor core axial length downstream of the OGV. A radial equivalent backpressure is assigned at the outlet boundary, but a constant backpressure value can also be used since the outlet flow is turned to the axial direction by the OGV. When approaching the stall limit, a step increase of backpressure of 200 Pa is used. The last converged point is taken as the numerical “stall” point.

The flow domain is discretized by hexahedron grids with an O4H topology, which are generated by using the Numeca AutoGrid5. In total, five sets of rotor and stator grids with different grid densities are generated. The mesh refinement is achieved by uniformly increasing the grid number to about 1.5 times in all dimensions, while the first layer grid displacement is kept the same at an area-averaged y^+ value around 1.1. Endwall features including gaps and fillets of the rotor and the stator are considered in the grid. Details of the grids are summarized in Table 2, and the grid topology is illustrated in Figure 2b. The OGV is meshed by a hexahedron grid with 0.8 million grid nodes, which has a similar grid density to the Medium grid of the rotor and the stator. Since the OGV does not have a pronounced effect on the upstream flow field, its grid density is kept the same throughout the paper. For a better representation of the computational grid, the Medium grid at the mid-span is presented in Figure 2c.

Results

Effect of grid density

In this section, five sets of uniformly refined grids (detailed in Table 2) are adopted to investigate the effect of grid density. Unless stated elsewhere, the rest of the numerical settings are kept the same, including the Ansys CFX solver, the SST turbulence model and the mixing plane rotor-stator interface model.

Table 2. Details of TUDa-GLR-OpenStage grids.

	Grid topology	UltraCoarse	Coarse	Medium	Fine	UltraFine
Rotor	Total radial grid point	37	53	81	121	181
	Tip gap radial grid point	9	13	21	33	49
	Hub fillet radial grid point	9	13	17	29	45
	Total tangential grid point	29	41	65	93	145
	Total axial grid point	41	61	97	141	213
	Boundary layer grid point	9	13	21	29	45
	Tip gap O-grid point	5	9	13	21	29
	Total grid point (million)	0.12	0.28	1.08	3.36	11.77
Stator	Total radial grid point	41	65	93	137	201
	Tip/hub fillet radial grid point	9	13	21	29	49
	Total tangential grid point	17	29	41	69	101
	Total axial grid point	37	53	85	129	189
	Boundary layer grid point	9	13	21	29	45
	Tip gap O-grid point	5	9	13	21	29
	Total grid point (million)	0.04	0.16	0.53	1.80	5.81

The stage performance characteristics at the design speed are presented in Figure 3, where the simulation results are represented by curves with open symbols, and the experimental data are denoted by solid squares with error bars. As the grid density increases, the characteristic curves gradually translate towards the top-right corner (i.e., higher pressure ratio, efficiency and mass flow rate; similar slopes of pressure ratio and efficiency curve). Excluding the UltraCoarse grid result, the stable flow range (SFR = $(m_c - m_s)/m_c \times 100\%$) increases with the grid density, from 8.7% of the Coarse grid result to 11.2% of the UltraFine grid result. When refining the grid

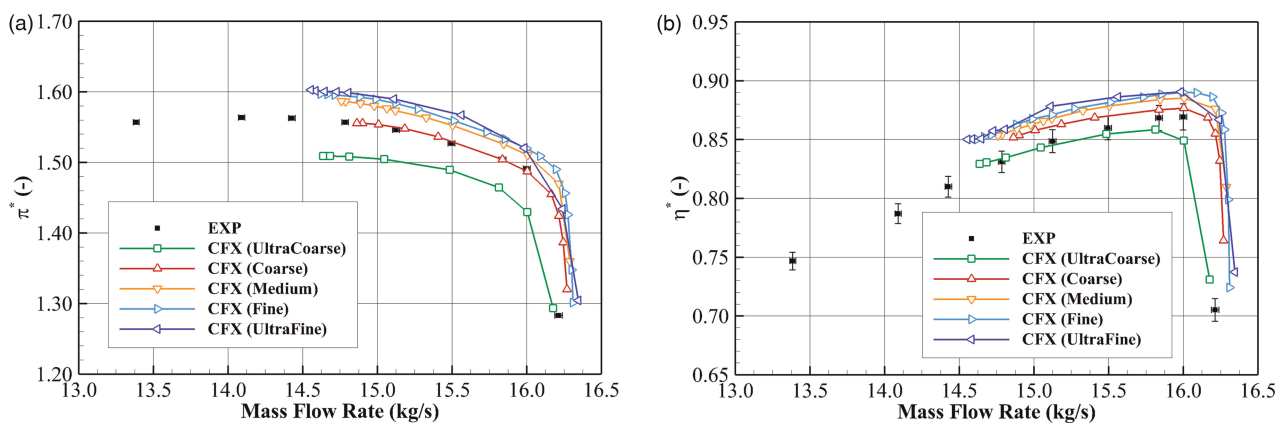


Figure 3. Effect of grid density on predicting the TUDa-GLR-OpenStage performance characteristics: (a) total pressure ratio and (b) isentropic efficiency.

to the Fine and UltraFine levels, the variation of pressure ratio and efficiency are within 0.01 and 0.1% respectively, indicating a grid-independent result. Note that although the results from the Coarse grid results match the best with the measured data, they are subjected to pronounced discretization error and thus cannot be taken as evidence of a good validation.

To examine the effect of grid density on the flow fields, the circumferentially mass-averaged radial profiles downstream of the stator are presented in Figure 4. In these plots, curves represent the numerical results obtained from the five grids, and solid squares denote the experimental results. For simplicity, only the PE results are presented. Results show that grid refinement leads to an increased total pressure ratio and total temperature ratio, especially at the upper 20% span. The Fine and UltraFine results are almost overlapping with each other, indicating grid independence has been achieved. However, they over-predict the total pressure ratio in the upper and lower 20% spans near the endwalls. Such a deficiency can be caused by the deficiency of the turbulence model, the deficiency of the mixing plane model, or plausible geometric uncertainties and errors. These factors will be examined later.

Following the concept of Roache (1998), the grid discretization error scales with Δ^n when using a n_{th} -order accurate advection scheme, where $\Delta = (1/N_g)^{1/3}$ is the nominal grid spacing with N_g the total number of grid points. For the second-order accurate schemes used in this work, a parabola can be fitted through the simulation results from different grids, i.e., $q = k\Delta^2 + q_{ideal}$, where k measures the grid convergence rate and q_{ideal} is the ideal simulation result free of discretization error. To check the grid convergence of different turbulence models and different solvers, the total pressure ratio and efficiency at the PE condition are plotted against Δ in Figure 5. In these plots, the solid square with error bars at $\Delta = 0$ denotes the experimental data, the rest scatters represent the simulation data obtained from the five grids, and the curves are the least-squares fitted parabolas.

Comparing the investigated five grids, the choice of grid density yields a 7% relative (to experiment) variation in total pressure ratio and a 7% absolute variation in isentropic efficiency. The discretization errors of the Fine grid, i.e., $|q_{ideal} - q_{Fine}|$, are about 0.01 in total pressure ratio and 0.5% in efficiency, which is adequately small. Therefore, the Fine grid will be used in later sections of the paper.

Comparing the investigated four turbulence models implemented in the two solvers, the choice of turbulence model yields a 5% relative variation in total pressure ratio and a 5% absolute variation in isentropic efficiency for the discretization-error-free values q_{ideal} at $\Delta = 0$. Specifically, the CFX(SST) method and the CFX(SA) method show similar prediction results, indicating both the SST-2003 and the SA-noft2 model are equally accurate in predicting this case. The Numeca(SA) method is evidently more sensitive to the grid density than the rest turbulence models, which is deduced to be caused by the fv3 version of the SA model.

Effect of Advection Scheme

In this section, the JST central scheme (Jameson et al., 1981) and the Roe upwind scheme (Roe, 1981) are compared with each other, both of which are second-order accurate. The rest of the numerical settings are kept the same, including the Numeca solver, the Fine grid, the SST turbulence model and the mixing plane rotor-stator interface model.

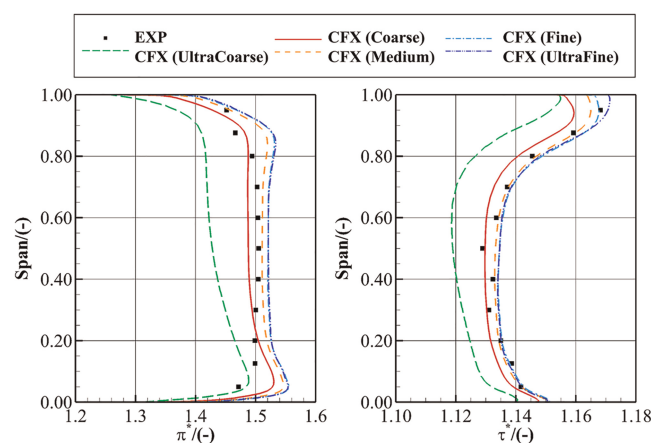


Figure 4. Effect of grid density on predicting the circumferentially mass-averaged radial profiles at the stage exit (ME30) at the PE condition.

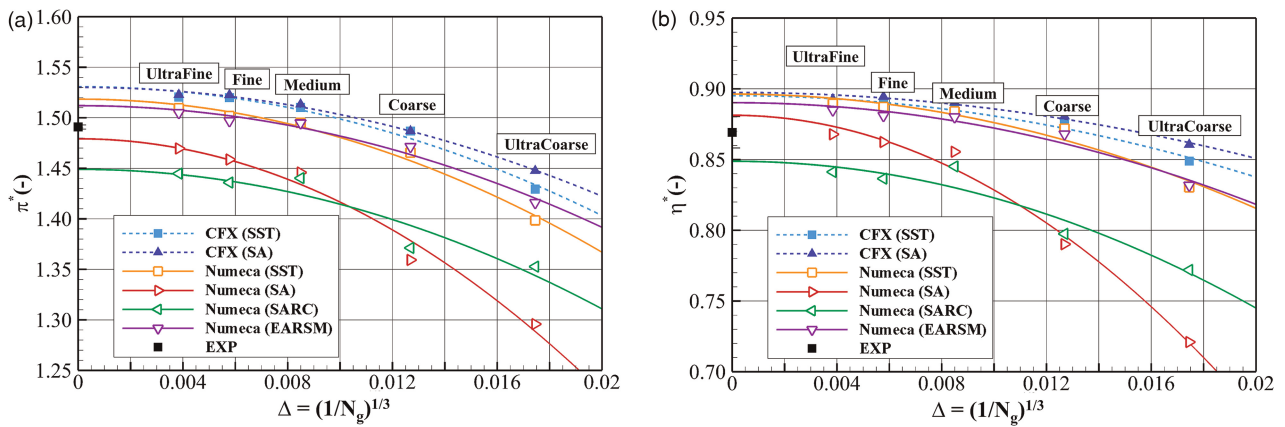


Figure 5. Grid convergence of TUDa-GLR-OpenStage at the PE condition using different turbulence models implemented in different solvers: (a) total pressure ratio and (b) isentropic efficiency.

The discretization error related to a second-order accurate advection scheme scales with the square of the grid spacing. Thus, the difference between the schemes is expected to be evident only when a coarse grid is used. In Figure 6a, the grid convergence of different advection schemes on predicting the compressor total pressure ratio at the PE condition is presented. It is confirmed that the choice of advection scheme has a negligible effect when refining the grid to the Fine grid level.

For a more detailed comparison, the grid convergence of different advection schemes on predicting the rotor suction surface shock front location is presented in Figure 6b. Here, the shock front is defined at the grid point where $\partial^2 p / \partial x^2$ reaches the maximum, and the fourth-order central finite difference method is used to calculate this derivative. The axial distance between the leading edge and the derived shock front location is then normalized by the axial chord length at the corresponding span, yielding the normalized shock front location X_{sf} . To represent the local grid density, the grid spacing of the adjacent grid cells is denoted by the error bars. Results show that the central scheme predicts the shock front slightly more upstream (i.e., by one grid spacing) than that of the upwind scheme when using the Coarse, Medium or Fine grid. This difference becomes indistinguishable when refining the grid to the UltraFine grid level.

For best practice, it is the choice of grid density rather than the choice of advection scheme that should be paid more attention to. Although any advection scheme can achieve an accurate prediction once the grid independence requirement has been met, a high-order scheme is still favorable in terms of computational cost.

Effect of turbulence model

In this section, four turbulence models namely SST, SA, SARC and EARSM are compared with each other. The rest of the numerical settings are kept the same, including the Numeca solver with the central advection scheme, the Fine grid and the mixing plane rotor-stator interface model.

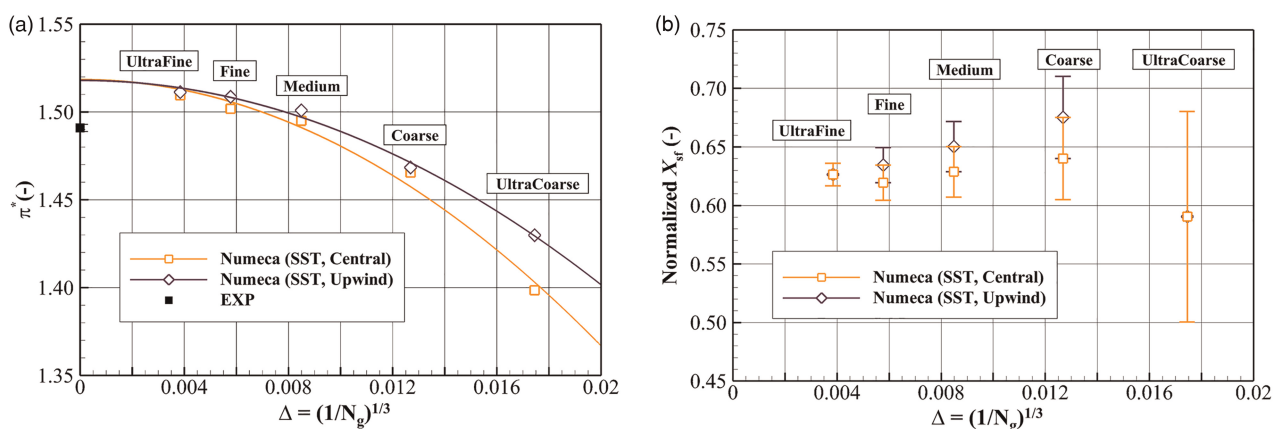


Figure 6. Grid convergence of TUDa-GLR-OpenStage at the PE condition using different advection schemes: (a) total pressure ratio and (b) normalized shock front location at 90% span of the rotor.

The stage performance characteristics at the design speed are compared with experimental data in Figure 7, where the measured data are represented by solid squares with error bars, and the simulation data are denoted by lines with scatters. In general, the SA model and the EARSM model predict the best agreement with the measured data. The SA model reproduces the stall margin² (SFR = 13.0% for the experiment; SFR = 14.3% for the SA prediction), the NS pressure ratio and the PE efficiency; however, the PE pressure ratio is under-predicted and the NS efficiency is over-predicted. The EARSM model accurately predicts the PE pressure ratio, but it under-predicts the stall margin (SFR = 9.6%) and slightly over-predicts the NS pressure ratio and the overall efficiency. The SST model predicts the highest pressure ratio and efficiency, but it is close to the EARSM results. The SARC model predicts the lowest pressure ratio and efficiency, which shows the least agreement with the measured data.

For further comparisons between the four turbulence models, the radial profiles at the rotor exit and the stage exit are examined in Figure 8. In these plots, simulation results are represented by lines, and the measured data are denoted by solid squares.

At the PE condition, both the SA model and the SARC model under-predict the pressure ratio and the flow angle at the rotor exit below 80% span, as shown in Figure 8a. Such deficiencies generally propagate to the stage exit shown in Figure 8b, which accounts for the under-prediction of the overall stage pressure ratio at the PE condition. The EARSM model and the SST model slightly over-predict the rotor exit pressure ratio above the 80% span and the rotor exit flow angle at full span, as presented in Figure 8a. At the stage exit shown in Figure 8b, the near-tip over-prediction of pressure ratio in the rotor passage is propagated to the stage exit; in addition, the near-hub over-prediction of pressure ratio arises, which is induced in the stator passage. These deficiencies of the endwall pressure ratio prediction, however, are too small to be observed in the overall stage pressure ratio shown in Figure 7a.

At the NS condition, the SA model predicts the most accurate pressure ratio profile at the stage exit, as shown in Figure 8d; the SARC model still under-predicts the pressure ratio at most spans, whereas the SST model and the EARSM model over-predict it especially near the endwalls. The shapes of all the pressure ratio profiles at the stage exit are similar to that at the rotor exit shown in Figure 8c, except that the SST result shows a total pressure loss near 80% span at the stage exit plane. This drop of total pressure corresponds to an excessive prediction of the corner separation size in the stator, as will be shown later. In terms of the stage exit total temperature ratio shown in Figure 8d, the EARSM model and the SST model show the best agreement with the measured data, whereas the SA model and the SARC model slightly under-predict it.

To complement the validation on the radial profiles, the total pressure ratio contours at the stage exit are presented in Figure 9. In these plots, the top row and the bottom row represent the PE condition and the NS condition, respectively; the columns from left to right represent the experiment, SST, SA, SARC and EARSM results.

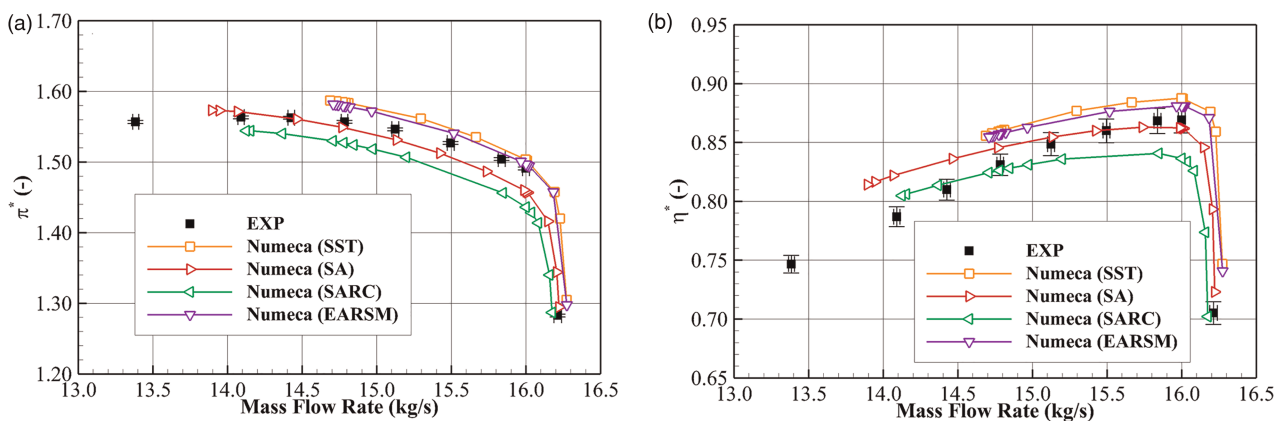


Figure 7. Effect of turbulence model on predicting the TUDa-GLR-OpenStage performance characteristics: (a) total pressure ratio and (b) isentropic efficiency.

2 For a fair comparison between experiment and CFD, the stall boundary is defined at the peak pressure ratio point.

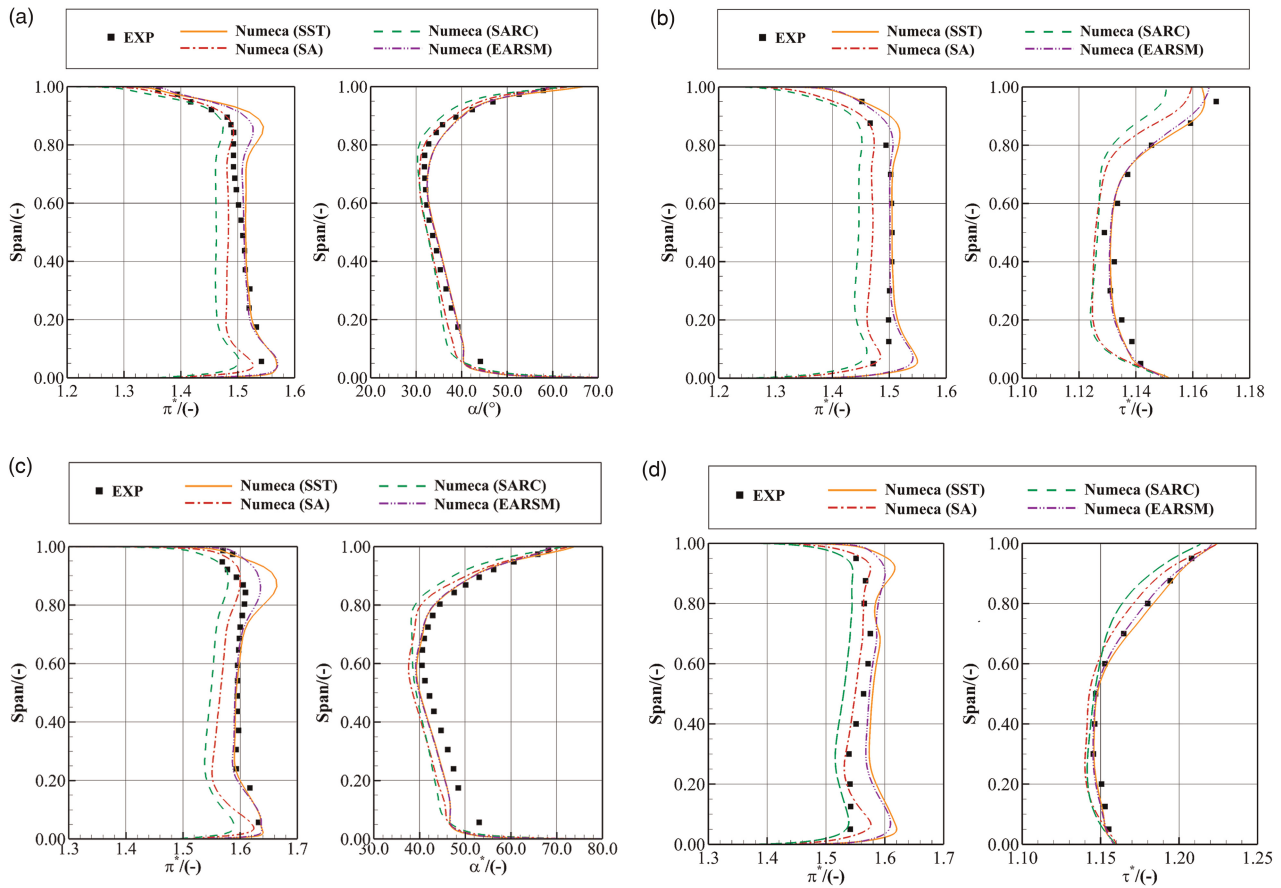


Figure 8. Effect of turbulence model on predicting the circumferentially mass-averaged radial profiles. (a) PE, rotor exit (ME21) (b) PE, stage exit (ME30) (c) NS, rotor exit (ME21) (d) NS, stage exit (ME30).

For the experimental results, a hub-suction surface corner separation is observed at both the PE and NS conditions, which is featured by low values of total pressure. As the compressor operates from PE to NS, the separation size increases. This corner separation, however, is not reproduced by any of the simulation results, leading to the near-hub over-prediction of the total pressure ratio observed previously in Figure 8b and d.

Among the simulation results, the SARC model and the SST model predict the lowest and highest overall total pressure ratio, respectively, which deviates from the measured data the most. The SST model also over-predicts the near-tip trailing edge separation size at the NS condition. Despite the EARSM model and the SA model predicting the best agreement with the measured data, evident differences still persist. Further investigations regarding the effect of the rotor-stator interface model and the effect of geometric uncertainties and errors (e.g., stator hub cavity leakage flow) are needed to improve the prediction accuracy.

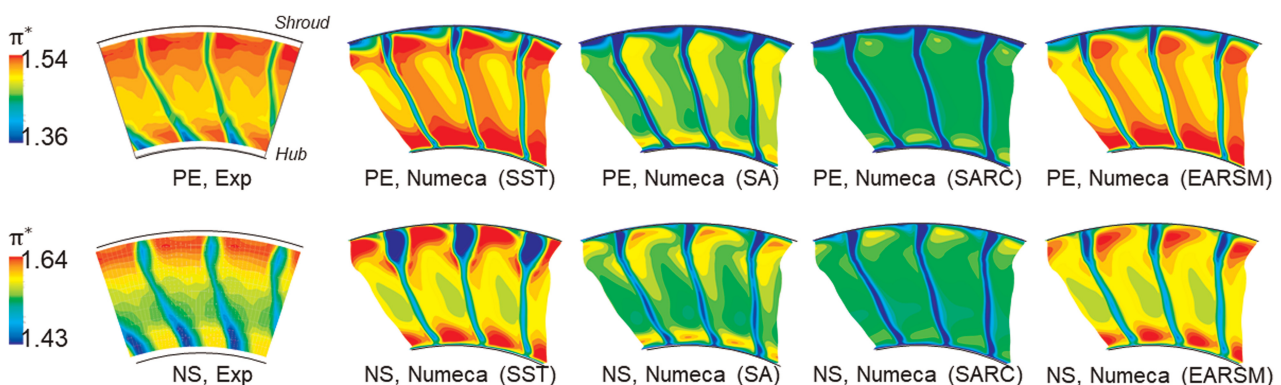


Figure 9. Effect of turbulence model on predicting the total pressure ratio contours at the stage exit (ME30).

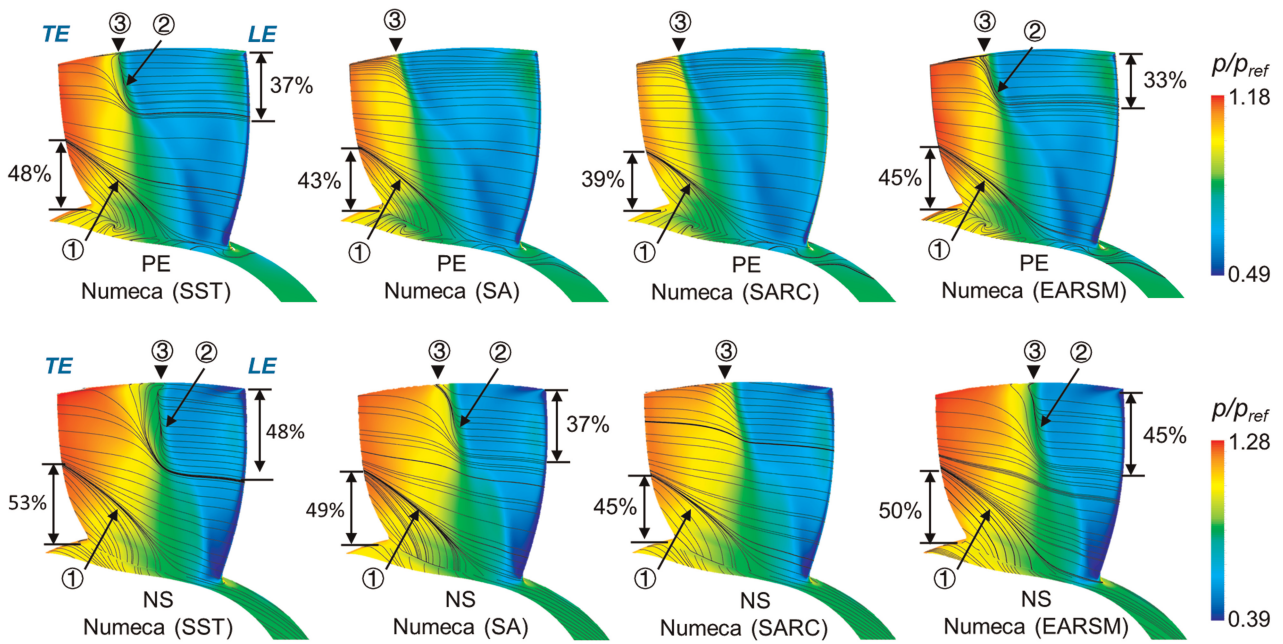


Figure 10. Static pressure contours and surface limiting streamlines on the hub surface and the suction surface of the rotor; ①: corner separation; ②: shock-induced separation; ③: shock front.

To compare the four turbulence models in predicting the rotor flow field, the static pressure contours superimposed with the surface limiting streamlines on the rotor suction surface are presented in Figure 10. In general, the rotor flow field is featured by a near-hub corner separation and a near-tip shock-induced separation. When the compressor is throttled towards stall, the shock front moves further upstream, and the sizes of both separation cells increase. Comparing the effect of turbulence models, the SST model predicts the largest separation size, followed by the EARSM, SA and SARC model. In particular, the near-tip shock-induced separation is not captured by the SA model at the PE condition, as well as the SARC model at both the PE and NS conditions. Such results imply that the SA and SARC models predict higher eddy viscosity in the rotor passage than the other models, which will be examined latter.

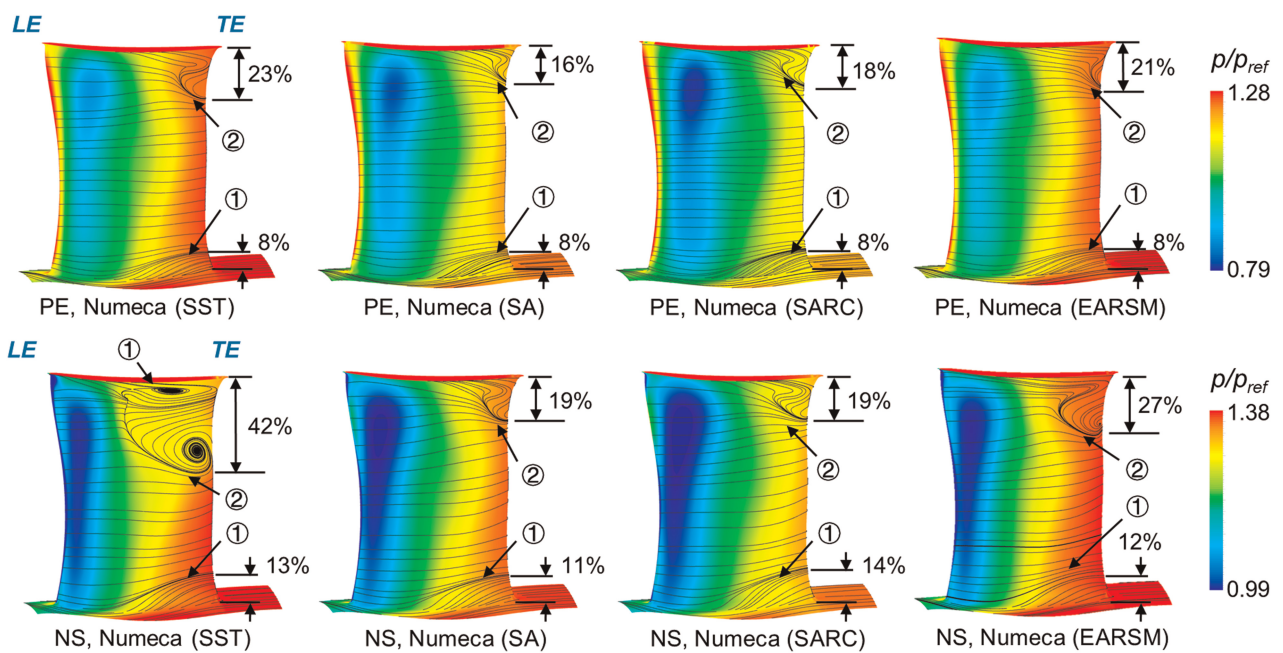


Figure 11. Static pressure contour and surface streamlines on the hub surface and the suction surface of the stator; ①: corner separation; ②: trailing edge separation.

To compare the four turbulence models in predicting the stator flow field, the static pressure contours superimposed with the surface limiting streamlines on the stator suction surface are presented in Figure 11. In general, the stator flow field is featured by a near-hub corner separation and a near-tip trailing edge separation. As the compressor operates toward stall, the sizes of both separation cells increase. Similar to the observations in the rotor flow fields, the SST model predicts the largest separation size, followed by the EARSM, SA and SARC model. In particular, at the NS condition, the SST model predicts a near-tip corner separation that connects with the trailing edge separation. This excessive prediction of separation size is consistent with previous observations in Figures 8d and 9.

To help understand the loss mechanism predicted by different turbulence models, the loss of efficiency ξ is monitored. The concept of loss of efficiency was originally introduced by Denton (1993) as an overall measure of compressor loss, i.e., $\xi = T_{t,e}(S_e - S_i)/c_p(T_{t,e} - T_{t,i}) \approx 1 - \eta^*$, where $T_{t,i}$, $T_{t,e}$, S_i , S_e are the total temperature and the entropy at the inlet and the exit, respectively. Later, it was extended to a scalar field $\xi(x)$ (He and Zheng, 2016), i.e., $\xi(x) = T_{t,e}(S(x) - S_i)/c_p(T_{t,e} - T_{t,i})$, where $S(x)$ is the entropy at an arbitrary location x .

The radial profiles of ξ at the stage exit (ME30) are presented in Figure 12. For the SST model and the EARSM model, their loss of efficiency profiles almost overlap with each other at the PE condition. However, the SST model predicts a higher loss near the 80% span at the NS condition, which corresponds to the excessive near-tip flow separation observed previously in Figure 11. For the SA model and the SARC model, they predict higher loss than the rest models below 70% span at both operating conditions, indicating the SA model and the SARC model predict a higher level of eddy viscosity and thus stronger skin friction on the blade surfaces. Such an effect on the eddy viscosity field will be confirmed later.

The investigated four turbulence models are all based on the concept of eddy viscosity. To help understand the behavior of the turbulence models further, the turbulent-to-laminar viscosity ratio contours are presented in Figure 13, where each row corresponds to an operating condition, and each column corresponds to a turbulence model. For the compactness of the figure, the inlet duct and the OGV are not shown.

For the two-equation turbulence models SST and EARSM, they are insensitive to the freestream eddy viscosity boundary condition (i.e., $\mu_t/\mu = 35$) assigned at the inlet of the simulation domain (not shown), as μ_t/μ dissipates to a small value before entering the rotor passage. Afterward, μ_t/μ develops with the rotor blade surface boundary layers in the mid-spans and with the tip leakage separation cell in the near-tip spans; the closer toward the NS condition, the higher the eddy viscosity level in the blade passage. When passing through the mixing plane interface, discontinuity of μ_t arises. Such a discontinuity is induced by the implementation of the mixing plane: conventionally, the two turbulence model quantities (e.g., k and ω in this case) are mixed out and thus are conservative across the mixing plane; when converting these quantities back to eddy viscosity (i.e., $\mu_t \sim k/\omega$), conservation of μ_t is not guaranteed. In this case, μ_t is abruptly increased immediately downstream

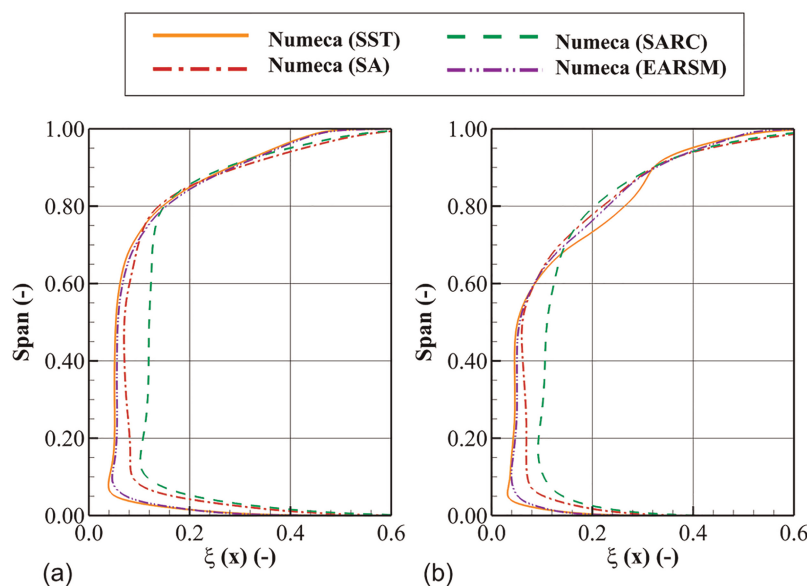


Figure 12. Circumferentially mass-averaged radial profiles of loss of efficiency at the stage exit (ME30): (a) PE condition; (b) NS condition.

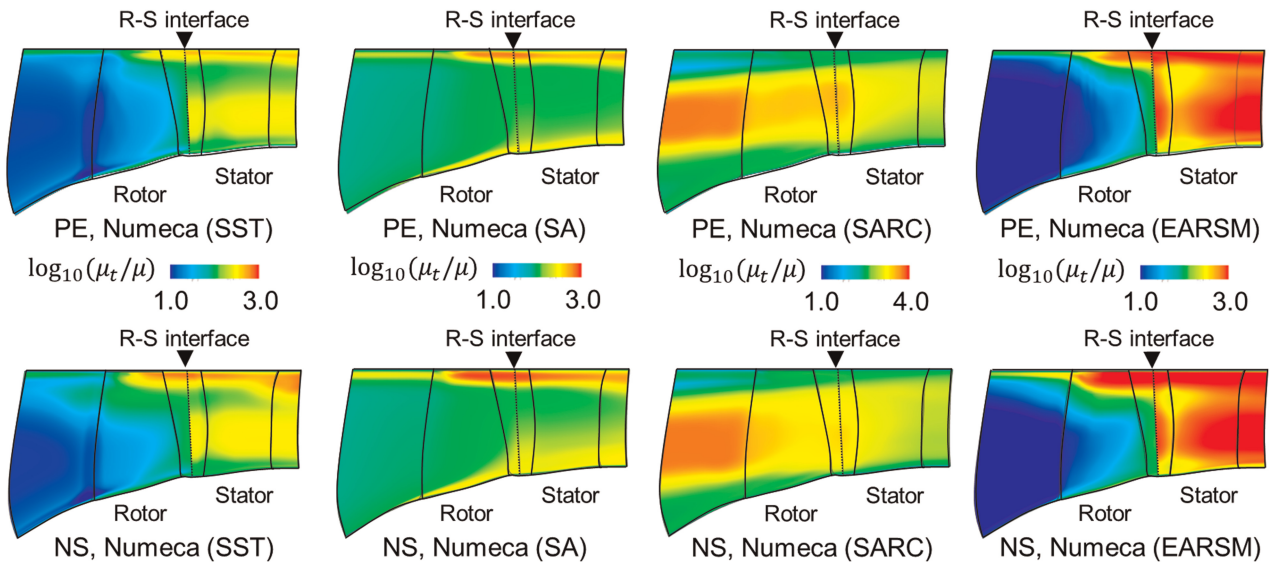


Figure 13. Circumferentially mass-averaged turbulent-to-laminar viscosity ratio contours.

of the mixing plane, which tends to reduce the separation size in the stator passage. For future research, it is recommended to test a mixing plane model that conserves μ_t and k across the interface.

For one-equation turbulence models SA and SARC, they are more sensitive to the freestream eddy viscosity as μ_t/μ increases by an order of magnitude before entering the rotor passage. The reason is that the dissipation term of μ_t depends purely on the wall distance and high μ_t/μ values in far-wall regions (e.g., farfield, freestream, etc.) cannot be dissipated effectively. As a result, the one-equation models predict a smaller separation size than the two-equation models in the rotor passage. The SARC model, in particular, predicts excessive values of μ_t upstream of the rotor passage. In the first place, these results were qualitatively reproduced by using an in-house flow solver (He et al., 2020) to rule out potential coding errors. By checking the formulation of the SARC model, it is found that the ν^* term goes infinitely large, which triples the production term of μ_t and thus the excessive μ_t at the inlet. This feature of the SARC model leads to an over-prediction of skin friction loss, an under-prediction of separation size, and hence the least accuracy in predicting the compressor performance and flow fields. Therefore, it is not recommended for axial compressor applications.

Effect of rotor-stator interface model

In this section, the mixing plane rotor-stator interface model typically used in steady simulations is compared with the sliding plane model used in unsteady simulations. The investigation is performed by using the Ansys CFX solver, the Fine grid topology and the SST turbulence model. To reduce the required computational resources, the number of stator blades has been changed from 29 to 32 so that a periodic sector of one rotor blade and two stator blades (1R2S) can be used for the sliding plane model. The time step used in the unsteady simulation corresponds to $\Delta t \cdot \text{BPF} = 48$, and the second-order backward Euler scheme is used for time stepping. The simulation has been performed over 6 rotor revolutions to reach a statistically steady state, and the data obtained in the last blade passing period is used for time averaging.

The stage exit (ME30) radial profiles obtained from the mixing plane method and the time-averaged sliding plane method are compared in Figure 14a. In the first place, the steady-state performances before and after changing the number of stator blades are compared with each other. It shows that both cases have almost the same profiles, indicating the scaling of the stator geometry barely changes the flow physics. Then, the sliding plane result is compared with the mixing plane result. No evident difference is found except that the sliding plane result shows slightly better agreement with the measured total temperature ratio. Such results indicate the mixing plane model is reasonably accurate at the investigated PE and NS conditions. Finally, comparing all CFD results with the measured data, the over-prediction of the stage pressure ratio in the upper and lower 20% span still persists. Such deficiencies are potentially caused by the geometric errors (as will be discussed in the later section) and the non-ability of RANS to sufficiently capture the turbulence effect of endwall flows.

To unveil the effect of the rotor-stator interface model on predicting the eddy viscosity field, the turbulent-to-laminar viscosity ratio contours are presented in Figure 14b. Results show that the mixing plane results have an abrupt increase of μ_t across the interface, whereas the time-averaged sliding plane results show a

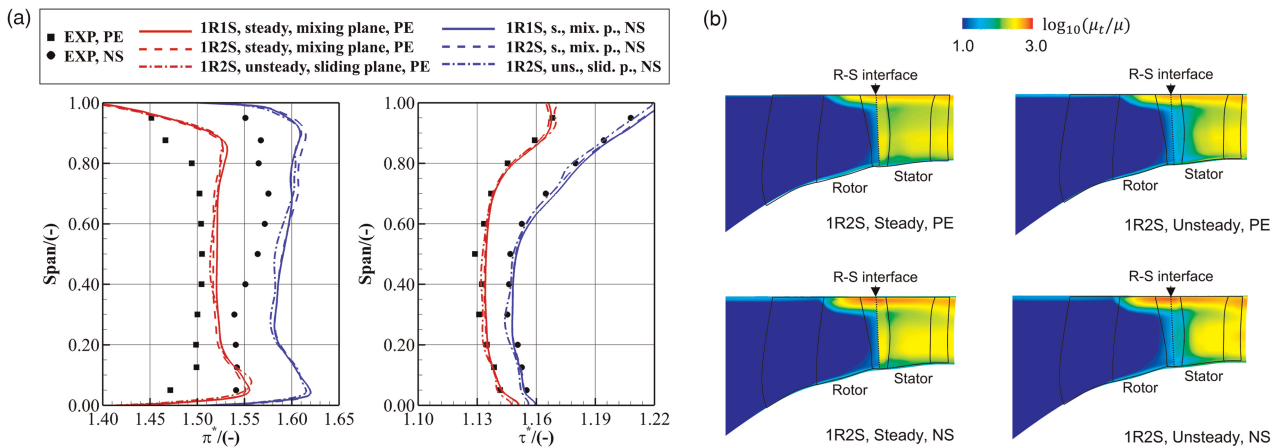


Figure 14. Effect of rotor-stator interface model on predicting the flow field at the PE condition. (a) Stage exit (ME30) radial profiles (b) Circumferentially mass-averaged viscosity ratio.

continuous distribution of μ_t across the interface, which is more reasonable. The difference of the overall μ_t distribution in the stator passage, however, is evident only near the stator leading edge. Such a difference will not have a visible effect on the downstream separation and thus the small difference in the mean flow field.

Discussions on geometric uncertainty and error

The above analyses are based on the assumption that the geometry used in the simulation is exactly the same as the one used in the experiment. In this section, the effects of some real geometry features are briefly discussed, including the rotor running tip gap shape, the rotor casing pinch and the stator hub cavity.

Effect of rotor running tip gap shape

In the experiment, the rotor running tip gap shape was measured by a capacitive blade tip timing system, and the tip gap size was found to increase by 0.2% C_t when throttling from the PE to the NS condition (Klausmann et al., 2021). To evaluate its effect on the predictions, the measured running tip gap shapes are simulated by using the Numeca solver with the central advection scheme, the Fine grid, the SST turbulence model and the mixing plane rotor-stator interface model. Results show that the difference in the stage total pressure ratio and the stage isentropic efficiency is only within 0.01 and 0.1% at both the PE and the NS conditions, which is consistent with previous research (Berdanier and Key, 2015). Therefore, the error induced by the running tip gap shape can be ignored in this case.

Effect of rotor casing pinch

In the experiment, a small pinch exists on the rotor casing endwall, but it is simplified as a smooth straight line in previous simulations. The shape of the pinch is illustrated in Figure 15a. In this section, the compressor with the realistic pinched casing is simulated by using the CFX solver, the Fine grid, the SST turbulence model and the mixing plane rotor-stator interface model. The radial profiles of the total pressure ratio are presented in Figure 15b. In general, the rotor casing pinch reduces the total pressure ratio at all spans, which improves the agreement with the measured data. This is because the pinched casing reduces the rotor throat area, increases the axial velocity (when comparing at the same mass flow), reduces the work input (by changing the rotor exit velocity triangle) and eventually reduces the total pressure ratio. Such a reduction effect is more evident in the PE condition than in the NS condition, because the slope of the total pressure ratio characteristic is steeper near the PE condition.

Effect of stator hub cavity

In the test rig, a secondary flow passage connects the stator inlet hub to the stator outlet hub, and a leakage flow may exist. To explore its effect on the prediction, a cavity geometry shown in Figure 16a is investigated numerically in this section. The simulation is conducted using the CFX solver, the Fine grid, the SST turbulence model and the mixing plane rotor-stator interface model. The total pressure ratio contours at the stage exit (ME30) are

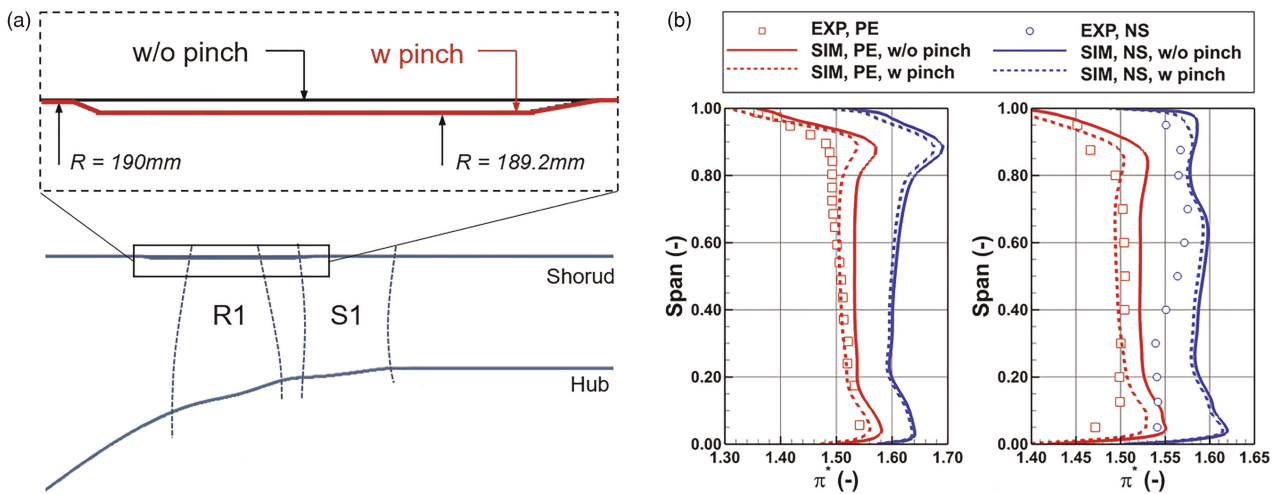


Figure 15. Effect of rotor casing pinch. (a) Illustration of rotor casing pinch (b) Radial profiles at the rotor exit (left) and the stage exit (right).

presented in Figure 16b. It shows that the stator hub cavity increases the near-hub total pressure loss at both the PE and the NS conditions, leading to slightly better agreement with the measured data. However, because the leakage mass flow rate of the investigated cavity geometry is only about 0.2% of the main flow rate, its effect is not strong enough to eliminate the near-hub disagreement with the measured data. According to previous research (Seshadri et al., 2015), a leakage mass flow rate of about 0.5% can potentially help match the measured data better. A parametric study of the cavity leakage flow rate will be pursued for future research.

Conclusions

A comprehensive validation and verification study of turbomachinery RANS flow solvers is conducted for the transonic axial compressor TUDa-GLR-OpenStage. Two commercial solvers namely Ansys CFX and Numeca FineTurbo are adopted to provide the benchmark solutions. Based on these solvers, five sets of grids, two advection schemes (i.e., central difference and second-order upwind), four turbulence models (i.e., SA, SA-RC, SST and EARSM) and two rotor-stator interface models (i.e., mixing plane and sliding plane) are investigated to quantify their effects on predicting the performance and the flow field of the compressor stage. Several conclusions are drawn as follows.

Among the investigated numerical setups, the choice of grid density and turbulence model has the most significant effects on the prediction. Specifically, the choice of grid density between 10^5 to 10^7 grid points per blade passage yields 7% relative variation in total pressure ratio, 7% absolute variation in isentropic efficiency, and 3% absolute variation in stable flow range; the choice of turbulence model among the investigated four models yields 5% relative variation in total pressure ratio, 5% absolute variation in isentropic efficiency, and 5% absolute variation in stable flow range. In contrast, the effect of the advection scheme on the compressor

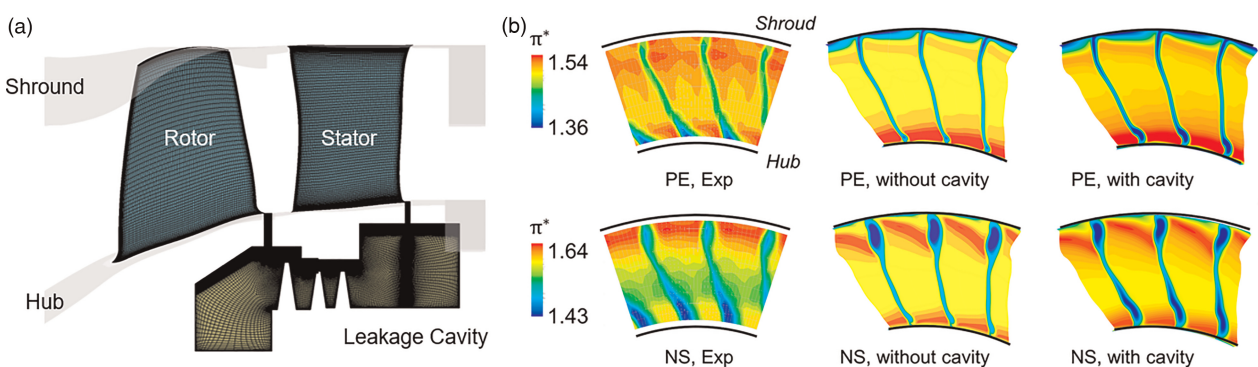


Figure 16. Effect of stator hub cavity. (a) Illustration of stator hub cavity (b) Total pressure ratio contours at the stage exit (ME30).

performance is not visible when using a refined mesh; the effect of the rotor-stator interface model is not evident either. These findings provide useful guidance for future RANS simulations of compressors.

Regarding the choice of grid density, the method from Roache (1998) has been demonstrated useful in estimating the discretization error of the current compressor, and it is recommended for future research. The current grid independence study shows that using about 1 million and 3 million grid points per blade passage can achieve a small discretization error in the global performance characteristics and the local flow fields, respectively. These numbers can be used as a rule of thumb for future RANS simulations. It is also demonstrated that the grid independence obtained from one turbulence model is transferable to another.

Regarding the choice of turbulence model, the EARSM model achieves overall the best accuracy and thus is recommended among the four models. Despite the SST model showing similar global performance characteristics to the EARSM model, it predicts the largest separation size and over-predicts the stator tip corner separation when operating near stall. The SA model over-predicts the eddy viscosity in the inlet duct, leading to the excessive loss of efficiency in the blade passages and thus the under-predicted total pressure ratio at the peak efficiency condition. The SARC model is the least accurate model due to the excessive prediction of eddy viscosity in the inlet duct, which leads to the smallest separation size, the largest friction loss and the lowest total pressure ratio and isentropic efficiency.

When using the grid density and the advection scheme with a small discretization error, none of the investigated turbulence models and the rotor-stator interface models can perfectly capture the measured compressor flow fields. The deficiency mainly comes from the near-tip flow of the rotor and the near-hub flow of the stator, which are likely related to the turbulence modeling deficiency in wakes/tip leakage flows/corner separations and the unknown geometric error near the stator hub. Future V&V works should focus on the verification and evaluation of RANS turbulence models with advanced features (e.g., nonlinear constitutive relation, transition, roughness, etc.), scale-resolving simulations and the real-geometry effects (e.g., stator hub leakage flow).

Data availability statement

The grids and the major CFD results presented in this paper will be uploaded to the GPPS workshop website.

Funding sources

Imperial College President PhD Scholarship (Grant Number: 01015425, Recipient: Xiao He). Henry Lester Trust (Recipient: Xiao He). The Great Britain-China Educational Trust (Recipient: Xiao He). Natural Science Foundation of China (Grant Number: 51906140, Recipient: Mingmin Zhu, Kailong Xia, and Jinfang Teng). National Science and Technology Major Project (Grant Number: 2017-II-0004-0017, Recipient: Mingmin Zhu, Kailong Xia, and Jinfang Teng).

Competing interests

Xiao He declares that he has no conflict of interest. Mingmin Zhu declares that he has no conflict of interest. Kailong Xia declares that he has no conflict of interest. Fabian Klausmann declares that he has no conflict of interest. Jinfang Teng declares that she has no conflict of interest. Mehdi Vahdati declares that he has no conflict of interest.

References

- ANSYS. (2021). *Ansys CFX—Solver Theory Guide, Release 20.1*.
- Ashford G. A. (1996). An Unstructured Grid Generation and Adaptive Solution Technique for High Reynolds Number Compressible Flows. PhD thesis, University of Michigan.
- Bakhtiari F., Wartzek F., Leichtfuß S., Schiffer H.-P., Goinis G., and Nicke E. (2015). Design and optimization of a new stator for the transonic compressor rig at TU darmstadt. In *Deutscher Luft- und Raumfahrtkongress 2015*.
- Berdanier R. A. and Key N. L. (2015). The effects of tip leakage flow on the performance of multistage compressors used in small core engine applications. *Journal of Engineering for Gas Turbines and Power*. 138 (5): 11.
- Bergner J., Kinzel M., Schiffer H.-P., and Hah C. (2006). Short length-scale rotating stall inception in a transonic axial compressor: experimental investigation. ASME Paper No. GT2006-90209.
- Computational Fluid Dynamics Committee. (1998). *Guide: Guide for the Verification and Validation of Computational Fluid Dynamics Simulations (AIAA G-077-1998 (2002))*. Reston, VA, USA: American Institute of Aeronautics and Astronautics.
- Denton J. D. (1993). The 1993 IGTI scholar lecture: loss mechanisms in turbomachines. *Journal of Turbomachinery*. 115 (4): 621–656. <https://doi.org/10.1115/1.2929299>
- Denton J. (1997). Lessons from rotor 37. *Journal of Thermal Science*. 6 (1): 1–13. <https://doi.org/10.1007/s11630-997-0010-9>
- Grosvenor A. D. (2007). RANS Prediction of Transonic Compressive Rotor Performance Near Stall. ASME Paper No. GT2007-27691.

- He X. and Zheng X. (2016). Mechanisms of lean on the performance of transonic centrifugal compressor impellers. *Journal of Propulsion and Power*. 32 (5): 1220–1229. <https://doi.org/10.2514/1.B36008>
- He X., Zhao F., and Vahdati M. (2020). Evaluation of spalart-allmaras turbulence model forms for a transonic axial compressor. GPPS Paper No. GPPS-CH-2020-0013.
- Hoeger M., Fritsch G., and Bauer D. (1999). Numerical simulation of the shock-tip leakage vortex interaction in a HPC front stage. *Journal of Turbomachinery*. 121 (3): 456–468. <https://doi.org/10.1115/1.2841338>
- Jameson A., Schmidt W., and Turkel E. (1981). Numerical solution of the Euler equations by finite volume methods using Runge Kutta time stepping schemes. AIAA Paper No. 81-1259.
- Klausmann, F., Franke, D., Foret, J., and Schiffer, H.-P. (2022). Transonic compressor Darmstadt - Open test case Introduction of the TUDa open test case. *Journal of the Global Power and Propulsion Society*. 6: 318–329. <https://doi.org/10.33737/gpps22-tc-71>
- Menter F. R. (1994). Two-equation eddy-viscosity turbulence models for engineering applications. *AIAA Journal*. 32 (8): 1598–1605. <https://doi.org/10.2514/3.12149>
- Menter F. R., Kuntz M., and Langtry R. (2003). Ten years of industrial experience with the SST turbulence model. In 4th International Symposium on Turbulence Heat and Mass Transfer, pp. 625–632.
- Menter F., Garbaruk A., and Egorov Y. (2012). Explicit algebraic reynolds stress models for anisotropic wall-bounded flows. *Progress in Flight Physics*. 3: 89–104. <https://doi.org/10.1051/eucass/201203089>
- Muller M. W., Schiffer H.-P., Voges M., and Hah C. (2011). Investigation of Passage Flow Features in a Transonic Compressor Rotor With Casing Treatments. ASME Paper No. GT2011-45364.
- NUMECA International. (2021). *Theory Guide—Fine/Turbo and Fine/Design3d 14.2*.
- Roache P. J. (1998). *Verification and Validation in Computational Science and Engineering*. Albuquerque, NM: Hermosa.
- Roe P. L. (1981). Approximate riemann solvers, parameter vectors, and difference schemes. *Journal of Computational Physics*. 43 (2): 357–372. [https://doi.org/10.1016/0021-9991\(81\)90128-5](https://doi.org/10.1016/0021-9991(81)90128-5)
- Rumsey C. L. (2021). *Turbulence Modeling Resource*. Hampton, Virginia, USA. Accessed August, 2021. <https://turbmodels.larc.nasa.gov/>
- Rumsey C., Smith B., and Huang G. (2010). Description of a Website Resource for Turbulence Modeling Verification and Validation. AIAA Paper No. 2010-4742.
- Seshadri P., Parks G. T., and Shahpar S. (2015). Leakage uncertainties in compressors: the case of rotor 37. *Journal of Propulsion and Power*. 31 (1): 456–466. <https://doi.org/10.2514/1.B35039>
- Shur M. L., Strelets M. K., Travin A. K., and Spalart P. R. (2000). Turbulence modeling in rotating and curved channels: Assessing the Spalart-Shur correction. *AIAA Journal*. 38 (5): 784–792. <https://doi.org/10.2514/2.1058>
- Spalart P. and Allmaras S. (1994). A one-equation turbulence model for aerodynamic flows. *Recherche Aerospatiale*. 1: 5–21.
- Suder K. L. (2021). NASA's role in gas turbine technology development: accelerating technical progress via collaboration between academia, industry, and government agencies. *Journal of Turbomachinery*. 143 (1): 011006. <https://doi.org/10.1115/1.4048696>